Electronic Supplementary Material (ESI) for Energy & Environmental Science.
This journal is © The Royal Society of Chemistry 2022

Supporting Information

A Sinter-Free Future for Solid-State Battery Designs

Zachary D. Hood,[1,#] Yuntong Zhu,[1] Lincoln J. Miara,[1,2] Won Seok Chang,[1,3] Philipp Simons,[1] Jennifer L.M. Rupp[1,4,*]

[1] Department of Materials Science and Engineering, Massachusetts Institute of Technology, Cambridge, MA 02139, USA

[2] Advanced Materials Lab, Samsung Semiconductor, Inc., Cambridge, MA, 02135, USA

[3] Samsung Advanced Institute of Technology (SAIT), Samsung Electronics Co., Ltd, Suwon, Korea

[4] Department of Electrical Engineering and Computer Science, Massachusetts Institute of Technology, Cambridge, MA 02139, USA

[#]Present address: Applied Materials Division, Argonne National Laboratory, Lemont, IL, 60439, USA

*Correspondence to: Jennifer L.M. Rupp (jrupp@mit.edu)

Methods

Materials and Synthesis of Spray Solutions. All the chemicals were used as received without further purification. $LiNO_3$ (≥ 99%), zirconium (IV) acetylacetonate (97%), and 1-methoxy-2-propanol (≥ 99.5%) were purchased from Sigma-Aldrich. $Al(NO_3)_3 \cdot 9H_2O$, $La(NO_3)_3 \cdot 6H_2O$ (99.99%), and bis(2-ethylhexyl) phthalate were purchased from Alfa Aesar. Methanol was purchased from VWR. Because of the hygroscopic nature of $LiNO_3$, this precursor was stored and massed in an argon-filled glovebox. Polished MgO (001) substrates (10 × 10 × 0.5 mm) were purchased from MTI Corporation. Spray solutions were prepared by dissolving stoichiometric ratios of Li, La, Al, and Zr salts in a methanol:1-methoxy-2-propanol:bis(2-ethylhexyl) phthalate (33:33:33 vol.%) solution, and all the spray solutions were stirred overnight for at least 12 hours.

Processing Garnet-based Electrolytes via SDS. Spray solutions were loaded into a polypropylene syringe and pumped at 10 mL/h into an atomizer (DeVILBLISS, AG361). The spray gun uses compressed air as the carrier gas with a pressure at the atomizer of 0.3 bar. MgO substrates were placed on a heated stainless-steel plate (on the surface of the hot plate). The substrate temperature was monitored with both an IR gun and a K-type thermocouple placed directly on the MgO substrate. During deposition, the temperature of the substrate surface was between 290 and 320 °C. The distance between the MgO substrate and atomizer was set to 24 cm. The spray solution was injected into the atomizer at a rate of 10 mL/h for all the data presented in this paper. For an image of the spray pyrolysis setup, please see Figure S1 in the supporting information. The sprayed films were post-processed in a MgO crucible at 600–800 °C in a temperature-calibrated tube furnace under a constant flow of pure O_2 (Airgas) at a heating/cooling rate of 10 °C/min. In order to ensure that the LLZO film remains dense and

continuous during the first step of the SDS process as well as the subsequent annealing procedure, the substrate remains flat and level with the heated surface or crucible.

Characterization of Crystal Structure, Microstructure, and Thermal Properties. After depositing the films, various *ex situ* and *in situ* techniques were used to analyze the formation of the different crystallographic phases. *In situ* X-ray diffraction with heating was completed on a PANalytical X'Pert Pro diffractometer with Cu-K_α radiation (λ = 1.5406 Å) equipped with an Anton Paar heating stage. For the *in situ* XRD measurements, the films were heated between 25 and 900 °C at a rate of 10 °C/min under pure O_2 (Airgas) with a 15-min isostatic dwell time before collecting the diffraction patterns. All the data were processed using HighScore Plus, a software package supplied by PANalytical. The near-order structure was evaluated using Raman spectroscopy (WiTec alpha 300 M+). All the Raman data presented in the paper were acquired with a power of 10 mW and a wavelength of 532 nm, together with a grating of 300 g mm^{-1} and a spectral resolution of 0.7 cm^{-1}. The Raman spectroscopy was also performed with *in situ* heating/cooling using a heating chamber (Linkam T95-HT; Linkam Scientific), operated between 25 and 1000 °C under pure O_2 (Airgas) with a heating/cooling rate of 10 °C/min; note that films were cooled to room temperature in the Linkam stage to improve the signal-to-noise ratio for Raman measurements. Note that the decrease in the Raman signal intensity below 80 cm^{-1} is an artefact of the equipment, which is due to the edge-filter cut-off for the laser wavelength (532 nm). The scanning electron microscopy (SEM) images were collected on a Zeiss Supra55VP field-emission scanning electron microscope operated between 3.0 and 10.0 kV using both the In-lens SE and the Everhart-Thornley SE detectors. The samples were cross sectioned with a diamond blade and attached to a specialized sample stage via carbon-conductive tape. The porosity of the films was determined by analyzing the surface and cross sectional SEM

images. The sprayed films were scraped from substrates and placed in MgO crucibles for differential scanning calorimetry (DSC), which was completed on a Mettler Toledo Thermal Analysis System TGA/DSC 3+ under a constant flow of air at a heating rate of 10 °C/min. X-ray photoelectron spectroscopy (XPS) spectra were collected for each powder sample on a Thermo K-Alpha XPS system with a spot size of 400 μm at an energy resolution of 0.1 eV. Ar^+ sputtering was performed with a beam energy of 4 eV, and the cluster size was 1000 atoms. All the XPS spectra were analyzed using Thermo Avantage, a software package provided by the manufacturer.

Electrochemical Characterization. Electrochemical impedance spectroscopy (EIS) of the sprayed Li garnets was performed using an in-plane geometry (Zahner IM6) by applying an AC amplitude of 50 mV with frequencies between 1 MHz and 0.1 Hz. Platinum (Pt) blocking electrodes (dimensions: 3.25 mm × 0.50 mm and an electrode separation of 0.25 mm) were deposited onto the Li-garnet films by DC magnetron sputtering (Kurt J. Lesker Company) and a stainless-steel shadow mask. For Arrhenius-type measurements, the Pt blocking electrodes were then contacted with Au-coated tungsten tips on a temperature-controlled stage (Linkam HFS-600E), and impedance spectra were collected between room temperature and 250 °C, which was monitored by a thermocouple placed directly on the surface of the film. The temperature was maintained for 15 min to equilibrate the substrate and film. The temperature was also carefully tuned to avoid any possible Li alloying between the Pt blocking electrode and the Li from the film. All the impedance spectra were collected under a constant flow of dry synthetic air. All the conductivity data were analyzed using ZView 3.4F.

***In Situ* Transmission Electron Microscopy.** High-resolution transmission electron microscopy (HR-TEM) was performed on an aberration-corrected FEI Titan S 8-300 TEM/STEM equipped

with a Gatan Image Filter Quantum-865 operated at 300 kV. The specimens were prepared by spraying 50–80-nm-thick films onto a MEMS-based heating chip (Protochips); a schematic of the heating chip is provided in the supporting information (Figure S7). A Protochips Aduro heating holder was used for all the *in situ* heating experiments. The specimens were heated at a rate of 10 °C/min with isothermal dwells of 0.5–60 min to evaluate the atomistic evolutions during the post-processing of the films. The electron beam was carefully tuned to minimize any electron-beam-induced damage to the films.

Supplemental Text:

Ionic conductivity of Li garnets in thin films: In most cases, techniques such as sol-gel-based or ALD-based depositions methods lead to ambient ionic conductivities on the order of 10^{-9} to 10^{-5} S/cm for the nanocrystalline films,[1-3] which are 3–5 orders of magnitude lower than those for Li garnets processed as macrocrystalline pellets or tapes via classic solid-state processing or tap-casting methods. One of the main issues for thin-film deposition of Li garnets is the fact that Li either does not efficiently transfer to the film during deposition (because of the high volatility of Li^+) or tends to diffuse out of the film during post-processing of the film. Recently, it has been shown that by including internal lithium reservoirs via a unique multilayer PLD-based technique using Li_3N, one can maintain fast deposition with the laser and obtain the high-conduction cubic phase ($\sigma_{Li^+} = 2.9 \times 10^{-5}$ S/cm at room temperature) and simultaneously drive the processing temperature to 660 °C, which is more than 400 °C lower than that of classic techniques based on tape casting or hot pressing[4] , which was further supported in follow-up work.[3]

Only a few reports describing wet-chemically-processed films of Li garnets employed sol-gel or dip-coating methods,[5-7] resulting in *thin films* of 40–300 nm in thickness. These films are clearly on the rather thin end of the processing spectrum, and their wide spread of ambient

Li^+ conductivities on the order of 10^{-9} to 10^{-6} S/cm at 25 °C and mixture of crystalline phases (tetragonal and/or cubic) indicate that the processing was not successful. Interpreting these reports is further challenged by their nature, as they are often first descriptions of synthesis chemistry and a reported phase and conductivity for dense film manufacturing of the SSB electrolyte ceramic. There is thus a lack of the type of insight needed to thoroughly understand *i)* the variables and their impact on the synthesis and densification chemistry and *ii)* the parameters that contribute to dry-cracking in the films.

On the basis of these first reports, it remains unclear whether the existing bridge between rather thin films below 1 µm and the lowest limit of screen-printed and sintered thick films of ~20 µm can be accessed using wet-chemical techniques to provide new opportunities for the manufacture of solid-state electrolytes. Careful analysis of these first reports based on sol-gel-based techniques indicates they do not yet yield thicker films for Li garnets, as it is difficult to control the drying as most of the metal salt precursors (e.g., zirconium (IV) acetylacetonate, $Al(NO_3)_3 \cdot 9H_2O$, $La(NO_3)_3 \cdot 6H_2O$ (99.99%), etc.) decompose often within a similar temperature window at *one event* during densification, leading to significant mass loss from the decomposition and prompting the formation of drying cracks, mixed phases (Li garnet and $La_2Zr_2O_7$), and ionic conductivities ranging from 10^{-9} to 10^{-6} S/cm. This sets an upper limit for effective precursor-to-metal-oxide mass transfer without rupture of the film in low-temperature densification, which has thus far made it impossible to access the desired thickness range above 1 µm. However, for facile SSB designs, this feat would be attractive and, if achieved, could provide suitable alternatives for low-temperature processing at low cost, opening up a path for manufacture without requiring sintering of the cells.

XPS analysis: Although we intentionally overlithiated the film by 75 mol.%, Li loss was expected at 750 °C, similar to that in previous thin-film studies of Li garnets.[2] Additionally, the XPS signal shows that the relative concentration of Li increases, in relation to the other elements, as the film is etched. This gradual increase in Li concentration could result from the melting of $LiNO_3$ at ~250 °C, forming a heterogeneous melt of amorphous oxides and liquid $LiNO_3$ during the post-processing at 250–360 °C. Gravitational forces may draw $LiNO_3$ towards the MgO substrate at temperatures between 250 and 360 °C, causing a slight deviation in the relative lithium concentration through the film. The bottom surface of the LLZO film (closest to the MgO) has 118% of the lithium of the top surface (directly under the surface carbonate layer), indicating the gradual concentration difference in lithium throughout the film. Another notable feature in the XPS depth profile is the slight deviation in O content as a function of depth, which could result from the formation of closed porosity in the film. The relative magnitude of this deviation was significantly more apparent in the O signal than in the Zr, Al, or La signal. Several important conclusions can be drawn from the XPS depth profiling. Quantitatively, the distribution of cations was relatively constant throughout the LLZO film, suggesting that the as-developed spray pyrolysis technique creates dense solid solutions on the surface of MgO. With increasing depth, the Li concentration slightly increased, suggesting that gravitational forces and Li^+ volatility play a significant role in the redistribution of Li during post-processing of sprayed LLZO films.

In situ XRD: We used X-ray diffraction (XRD) with *in situ* heating to analyze the phases of an as-deposited film with a nominal thickness of 10 ± 0.9 μm and overlithiation of 75 mol.% as a function of temperature and time, Fig. S5. Each pattern was collected with a ramp rate of 10

°C/min and a 30-min isothermal step before data collection. From 300 to 400 °C, the film was mostly amorphous, signifying that the metal salts either melted or decomposed on the surface of the MgO substrate. From 500–600 °C, several crystalline peaks emerged at 2θ = 28.2°, 32.5°, 47.2°, and 56.8°, corresponding to the (222), (400), (440), and (622) planes of the $La_2Zr_2O_7$ pyrochlore phase, respectively. At 650–700 °C, the tetragonal phase of the garnet appeared, yet remnants of the pyrochlore can still be detected in the XRD patterns. When the film was further heated to 750 °C, the cubic phase of the Li garnet emerged, which closely agrees with the ICSD structure 183607. The *in situ* XRD results signify that the cubic phase was retained to 850 °C. Upon ramping to 900 °C, the film converted back to the $La_2Zr_2O_7$ pyrochlore phase, presumably due to significant Li loss at this temperature. These results collectively signify that it is possible to attain phase-pure cubic Li garnet films by over-lithiating the films with 75 mol.% excess lithium and annealing the films for 30 min under O_2. No peaks for the MgO substrate were observed at any point during the experiment, signifying that the substrate was homogenously covered by the Li garnet. It is central to SDS that the Li salt decomposes within the first formed amorphous and pyrochlore structure; however, in the temperature ranges of the current XRD experiments (300–900 °C), crystalline $LiNO_3$ was not observed.

Differential scanning calorimetry: We performed differential scanning calorimetry (DSC) of as-sprayed films (overlithiation of 75 mol.%) to better understand the dynamic processes involved in the second step of SDS. As seen in the DSC curve in Figure S6, several notable endothermal and exothermal events occurred in the films when heated under synthetic air (flow rate: 10 mL/min) at a ramp rate of 10 °C/min. The first endothermal peak, occurring at ~250 °C, is related to $LiNO_3$ melting in the film. The next exothermal peak, with an onset temperature of ~360 °C, is

related to the decomposition of the nitrates in the film. At a heating rate of 10 °C/min in an atmosphere of dry synthetic air, it is apparent that all of the nitrate decomposes when the film is heated to 400 °C. In its pure form, $LiNO_3$ will decompose in air at approximately 580–600 °C. Here, the decomposed metal salts in the film (*e.g.* Al, La, and Zr) are believed to catalyze the decomposition of the nitrate from $LiNO_3$ at significantly lower temperature. In fact, XPS analysis of the films annealed at 450 °C for 30 min (heating/cooling rate of 10 °C/min) shows that no nitrate is present in the film, supporting the aforementioned decomposition mechanism (Figure 2 in the main text). The second endothermic event at 525–625 °C in the DSC curve corroborates the crystallization of LLZO. Taking the thermal analysis into account, we first set the post-processing temperature of lithium garnets to 750 °C under a flow of pure O_2 in order to decompose any residual nitrates in the film as well as crystallize the Li-garnet films.

Control of lithiation toward the desired phase: It is known from earlier Li SSB science that in particular fast-conducting electrolytes require fine control of their lithiation degree to stabilize the desired phase, see discussion in Ref. [8]. This is often a painful process as for all fabrication methods involving sintering, it requires over-lithiation of the powder prior to sintering (due to the high volatility of Li), and in vacuum techniques such as PLD, it requires the same for the pellet. There is an existing limit on how much Li can be pushed into a sintered ceramic body, and too high of a load (e.g., 20 mol.% for Li garnets) results in crumbled and porous structures. An interesting topic to explore through this research is how strongly one can adapt the overlithiation without damaging the densification process and drying when steering it to have the $LiNO_3$ be present as a salt at deposition and during the formation of the $La_2Zr_2O_7$ pyrochlore phase and decomposing at higher temperature: *what is the limit? And how does the post-lithiation work for*

this type of ceramic synthesis? To answer these questions, we investigated the 2-step SDS process to control drying and probe the upper thickness manufacturing limits, investigate the decomposition of the Li salt in a formed pyrochlore structure, understand the role of over-lithiation and settings for phase evolution via this new synthesis approach, and probe the final structure–transport properties for cubic $Li_{6.25}Al_{0.25}La_3Zr_2O_{12}$.

Taking a closer look at the microstructure of the films (Figure 3) prepared via spray pyrolysis and Li garnets prepared by classic thin film techniques (*e.g.* PLD, sputtering) or bulk techniques (*e.g.* tape casting, hot pressing), the average grain size to solid-electrolyte thickness aspect ratio differed significantly between these techniques, as shown schematically in Figure S8. Traditional vacuum-based thin-film approaches generally yield films with a thickness of 0.4–0.7 μm, together with an average grain size of 0.005–0.050 μm. In contrast, tape casting generally yields films between 25 and 100 μm in thickness with an overage grain size of approximately 2–10 μm. Sintered pellets of Li garnets are usually between 150 and 1000 μm in thickness, with an average grain size of approximately 20–80 μm. In the as-developed spray method, the Li-garnet films range from 1–10 μm in thickness, with an average grain size of 0.01–0.080 μm. Such a microstructure as seen in the sprayed Li-garnet film is incredibly unique among Li garnets, and this microstructure is also expected to affect their electrochemical performance.

It should be mentioned that all of the aforementioned films were between 0.04 and 1.0 μm in thickness. In the present study, we were able to grow significantly thicker films of Li garnets ranging from 1–10 μm in thickness, which also exhibited among the best Li^+ conduction and low E_a. The low processing temperature, relatively fast deposition for growing Li-garnet

films, and the ability to access significantly thicker films represent obvious advantages of the as-developed spray pyrolysis technique, holding many enticing possibilities for upscaling.

***Electrochemical impedance spectroscopy*:** The LLZO-based films were post-processed at 750 °C for 30 min (ramp rate: 10 °C/min) under a flow of pure O_2. EIS spectra were collected with an in-plane geometry with Pt blocking electrodes (as shown schematically in the inset of Figure S9a) and under a flow of synthetic air between 30 °C and 185 °C. Representative Nyquist plots are shown in Figure S9a, where the amplitude was varied from 50 to 1000 mV to rule out any contributions from the Pt blocking electrode. Here, it can be seen that the spike from frequencies between 1 and 0.001 Hz does not significantly change, meaning that the diameter of the semicircle can be taken as the total conductivity in the films at the measured temperature. A strong overlap was observed between the grain bulk and grain-boundary contributions in the Nyquist plots; thus, it was not possible to separately quantify these contributions. Because of this challenge in data analysis, we used a resistor in parallel with a constant phase element for the fitting to represent the total Li^+ conductivity in the films.

The calculated conductivities are presented in an Arrhenius representation (Figure 3 in the main text) with respect to the effective lithiation given in mol.% of the initial spray solution for the film ranging from 10 to 125 mol.% excess Li, and the effect of overlithiation on these electrochemical properties in light of the microstructure and phase are presented in Figure S9b. The films grown from a spray solution with an overlithiation of 75 mol.% possessed the highest Li^+ conductivity of $2.4 \pm 0.05 \times 10^{-6}$ S/cm at 30 °C and $1.5 \pm 0.05 \times 10^{-4}$ S/cm at 185 °C, together with an Arrhenius activation energy (E_a) of 0.34 ± 0.03 eV. Nevertheless, the E_a of the films from SDS was slightly higher than that reported in tape-cast or pellet-based studies (0.28–

0.33 eV).[9-10] In comparison, the films deposited from a spray solution with 10 mol.% excess Li had no measurable ionic conductivity between 30 and 90 °C and an ionic conductivity of 8.2 ± 0.05 × 10^{-8} S/cm at 185 °C and 4.1 ± 0.05 × 10^{-6} (E_a = 0.44 ± 0.04 eV), possibly due to the formation of off phases (*e.g.* tetragonal-like and delithiated $La_2Zr_2O_7$ pyrochlore phases). The films prepared with spray solutions with 250 mol.% excess Li had no measurable in-plane ionic conductivity within the temperature range explored, possibly due to the significant porosity in the film. To further evaluate the effect of the lithiation of the spray solution on the resulting electrochemical properties of the films, we prepared two additional spray solutions with an overlithiation of 30 and 125 mol.% Li and deposited these solutions as Li-garnet films using the same post-processing conditions as the aforementioned films. The solution with 30 mol.% excess Li yielded an ionic conductivity of 4.3 ± 0.05 × 10^{-7} S/cm at 30 °C and 7.2 ± 0.05 × 10^{-5} S/cm at 185 °C, together with an E_a of 0.38 ± 0.04 eV. This decrease in the ionic conductivity could be due to less lithium incorporation into the film, leading to off phases similar to those seen in films prepared from spray solutions with 10 mol.% over-lithiation. Increasing the over-lithiation of the spray solution to 125 mol.% yielded films with an ionic conductivity of 1.2 ± 0.05 × 10^{-6} S/cm at 30 °C and 9.5 ± 0.05 × 10^{-5} S/cm at 185 °C, together with an E_a of 0.36 ± 0.04 eV. Compared with the films prepared from a spray solution with 75 mol.% lithium, the change in conduction was small, signifying that spray solutions with 75–125 mol.% over-lithiation will produce Li-garnet films with similar, yet controllable, electrochemical properties.

Figure S10 presents an Arrhenius plot of the properties of Li garnets prepared by various thin-film techniques. Most conventional vacuum-based growth of Li garnets yield thin-film Li garnets with thicknesses between 0.04 and 0.7 μm and ionic conductivities <10^{-6} S/cm. Li garnets prepared by RF magnetron sputtering yield films with ionic conductivities ≤ 10^{-6} S/cm at

room temperature.[11-16] Similarly, the best thin-film Li garnets prepared via atomic layer deposition (ALD) have a low ionic conductivity of 7.8×10^{-5} S/cm at 200 °C and 1.2×10^{-6} S/cm at 100 °C.[1] Classic PLD approaches from single LLZO-based targets generally yield thin films of Li garnets with significantly lower ionic conductivities ($< 10^{-8}$ S/cm at room temperature).[2, 17] A newly developed PLD approach, which involves internal lithium reservoirs via a unique multilayer PLD-based technique, shows that one can maintain the high-conduction cubic phase together with a Li^+ conductivity of 2.9×10^{-5} S/cm at room temperature.[4] Apart from the vacuum-based techniques, wet-chemical processes such as classic sol-gel methods produce thin films with an ionic conductivity on the order of 10^{-9}–10^{-6} S/cm at room temperature.[5-7]

Supplemental Figures and Tables

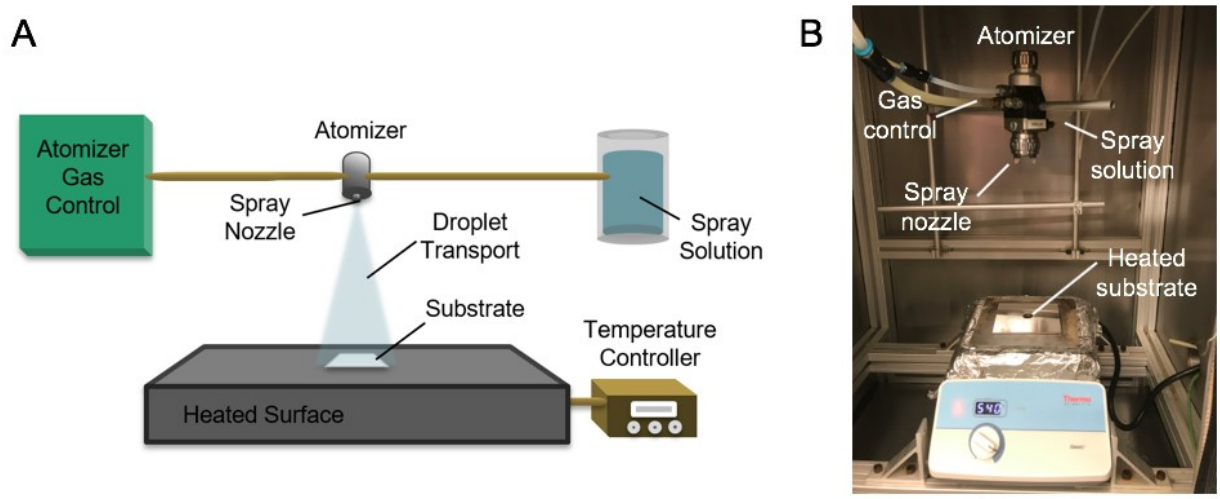

Figure S1. A) Schematic representation and B) image of the spray pyrolysis setup to grow Li-garnet films. Our spray chamber has several key features: 1) the hot plate can be heated up to 540 °C, allowing for the surface of the substrate to reach as high as 350 °C (under proper spray conditions), 2) the atomizer can run at pressures up to 3 bar, and 3) the spray solution can be injected as slow as 5 mL/h and as fast as 30 mL/h via a syringe pump.

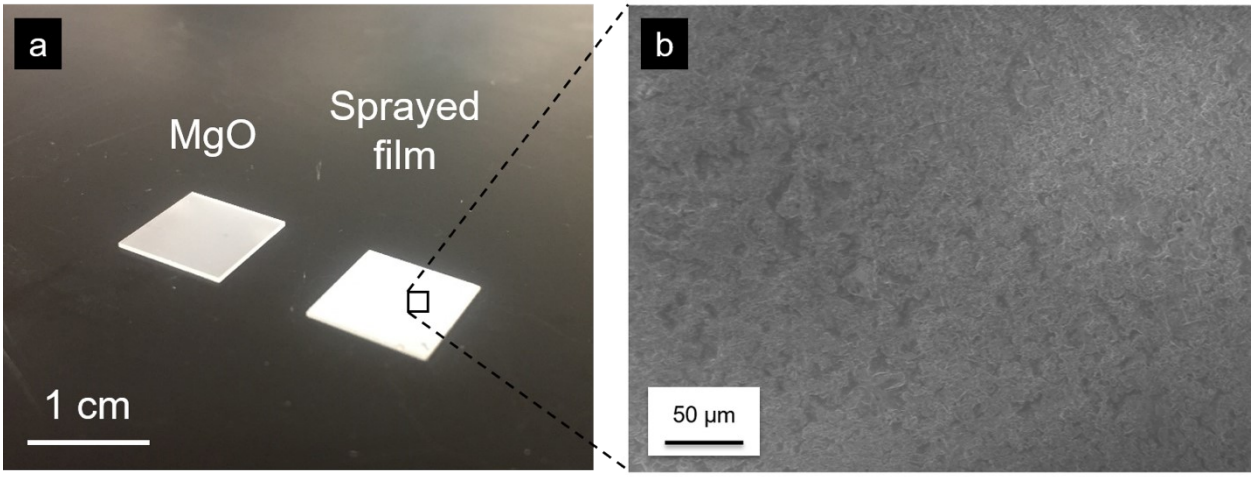

Figure S2. A) Image of an MgO substrate before and after an ~6-µm-thick Li garnet was processed via SDS (*e.g.,* the spray solution was first deposited onto the heated substrate and annealed at 750 °C under a flow of pure O_2). B) SEM micrograph of the surface of a sprayed Li-garnet film after annealing at spraying and after 750 °C under a flow of pure O_2.

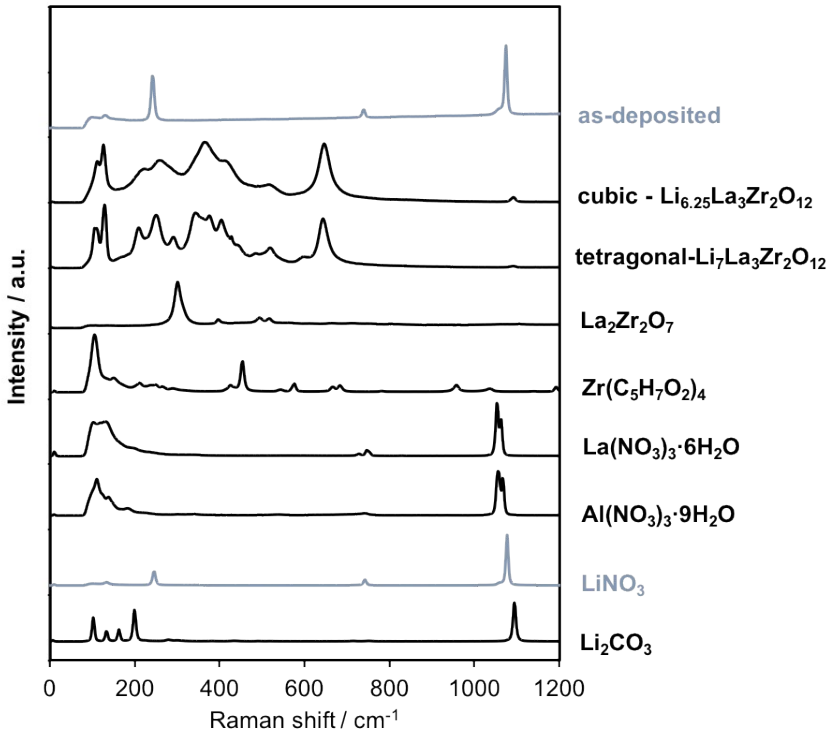

Figure S3. Raman spectra of as-deposited films of Li garnets (overlithiation: 75 mol.%).

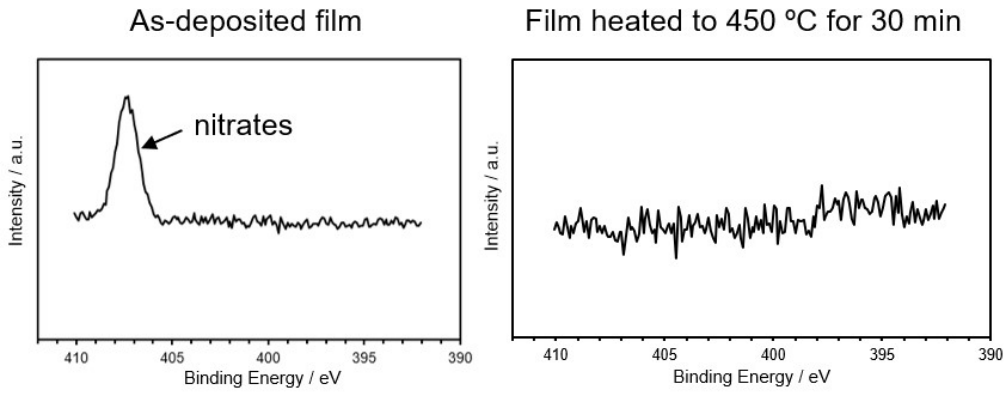

Figure S4. XPS analysis of the N1s region for a sprayed film (heated at 280 °C) and an annealed film (heated to 450 °C under O_2 for 30 min). Nitrogen is still present in the sprayed films after depositing the spray solution with a surface temperature of 280–330 °C, suggesting that some of the precursors (namely the $LiNO_3$) did not fully decompose during spray pyrolysis.

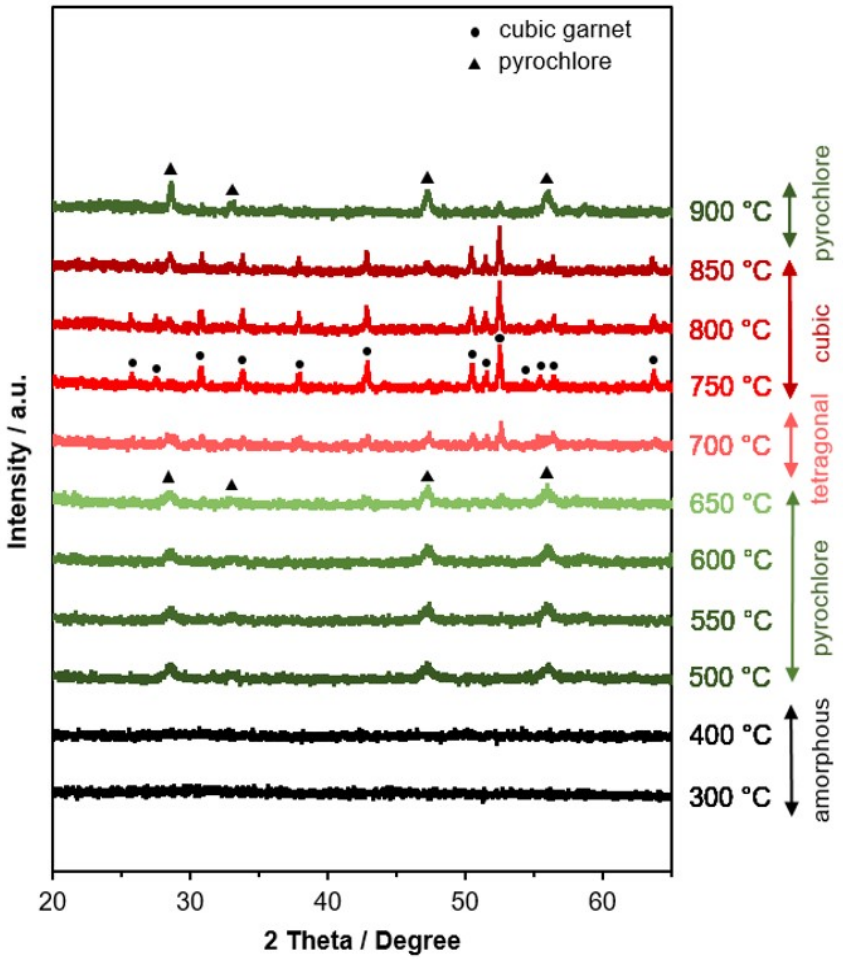

Figure S5. *In situ* XRD patterns of the sprayed Li garnet films with 75 mol.% excess Li.

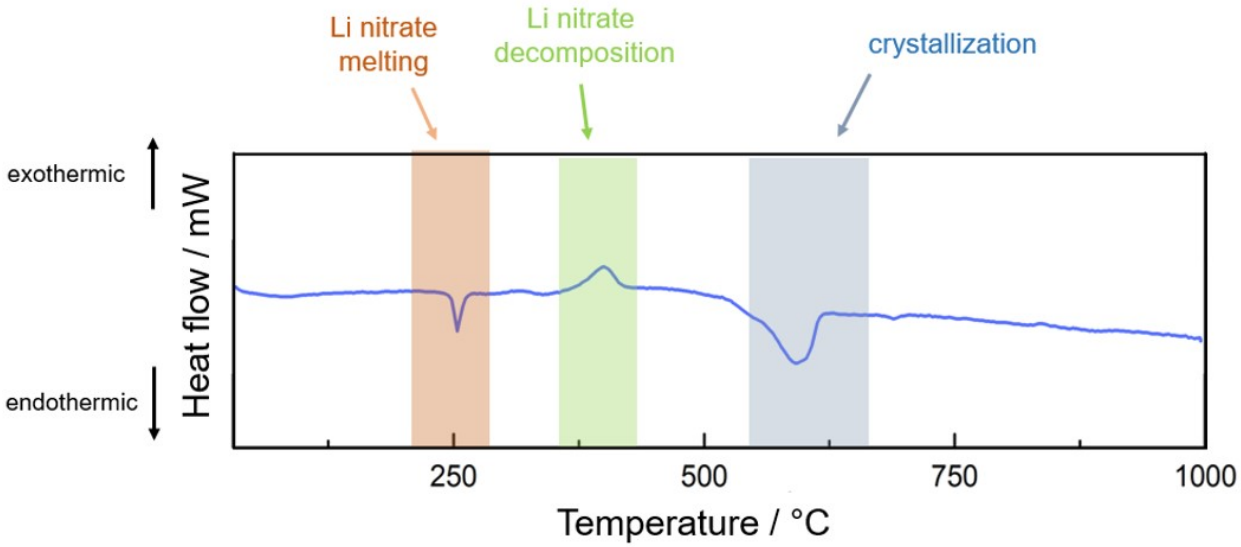

Figure S6. DSC curve of an as-sprayed lithium-garnet film (overlithiation: 75 mol.%) under a flow of synthetic air at a ramp rate of 10 °C/min. The first endothermic event is related to melting of $LiNO_3$, the first exothermic peak is related to the decomposition of nitrates, and the last endothermal peak is related to the crystallization of the Li-garnet film.

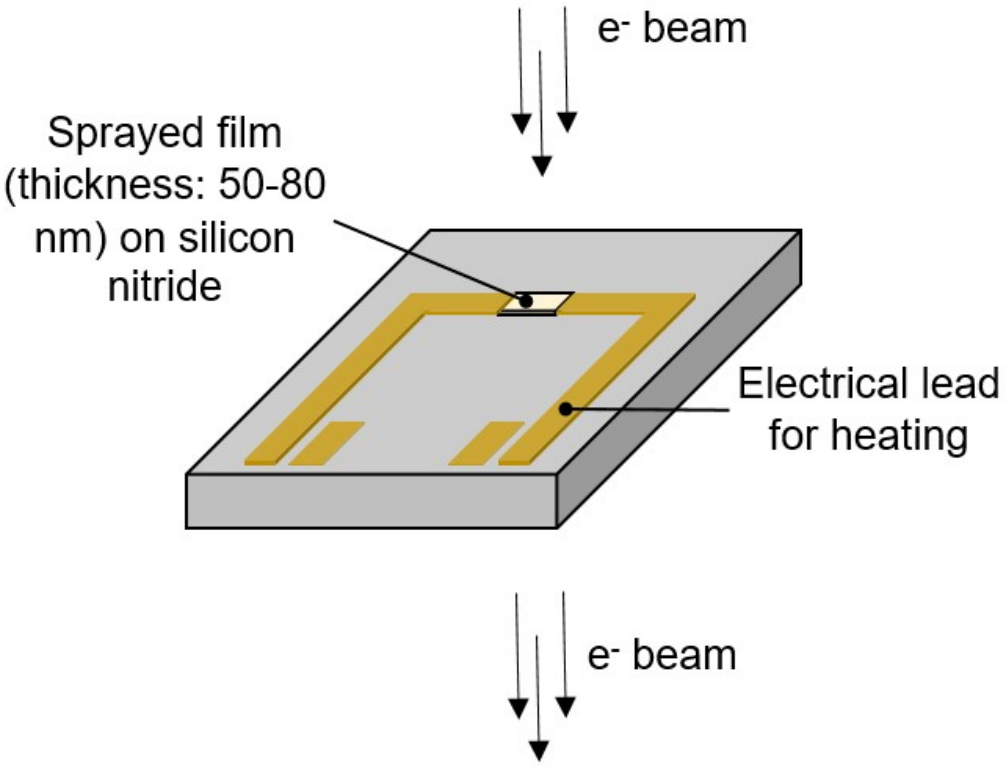

Figure S7. Schematic representation of chip used to study the crystallization of sprayed Li-garnet films.

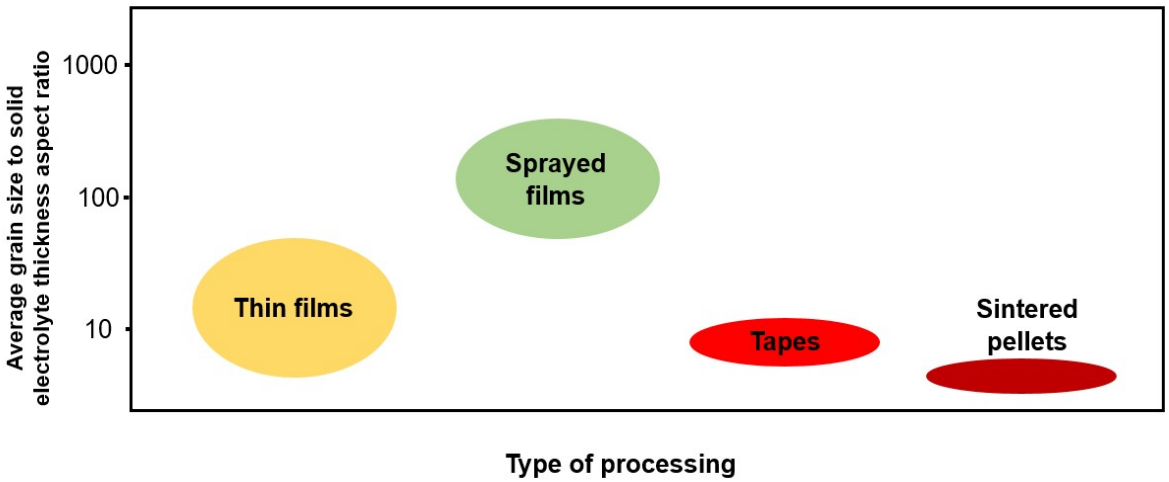

Figure S8. Average grain size to solid-electrolyte thickness aspect ratios of thin films, sprayed films, tapes, and pellets.

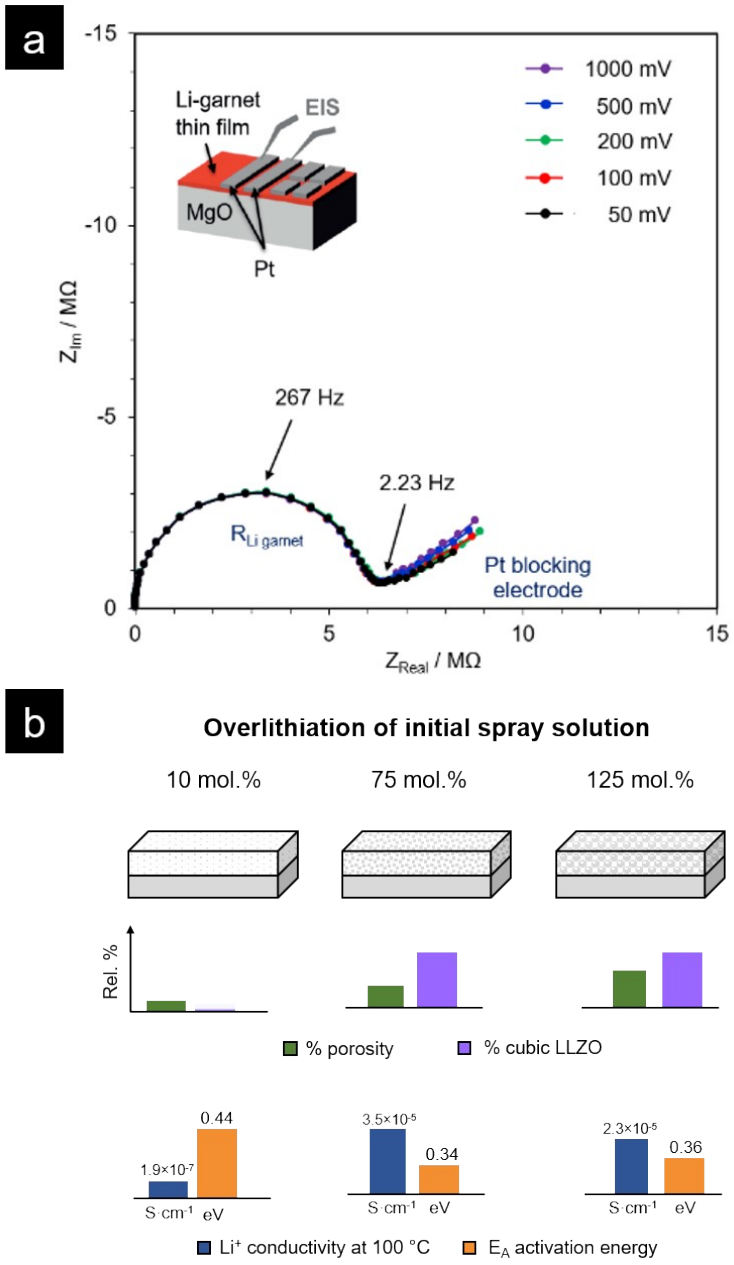

Figure S9. A) Representative Nyquist plots of EIS of the sprayed films. B) Schematic representation showing the effect of the phase and microstructure on the Li^+ conductivity and Arrhenius activation energy.

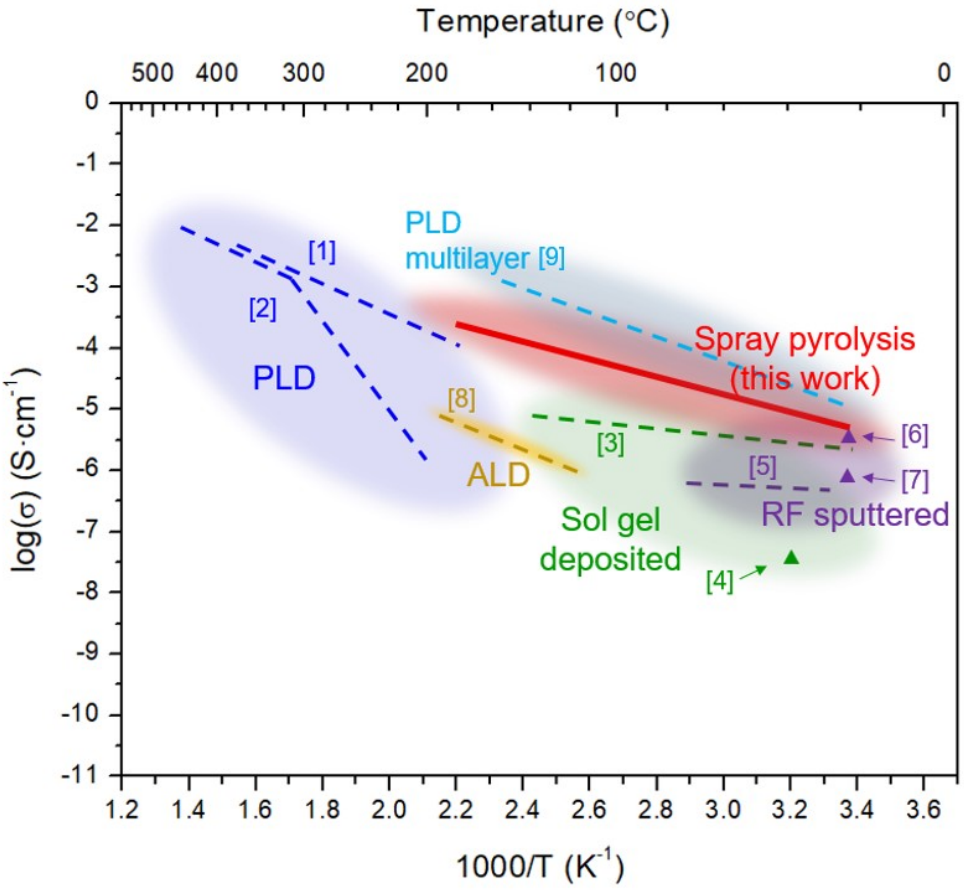

Figure S10. Overview of the ionic conductivity of the highest-conducting sprayed Li-garnet films compared with that achieved using other reported Li-garnet thin-film techniques. (**References:** [1] Park et. al. *Thin Solid Films* 2015, *576*, 55. [2] Rawlence et al. *Nanoscale* 2014, *8*, 14746. [3] Chen et. al. *J Mater. Chem. A*, 2014, *2*, 13277. [4] Bitzer et. al. *Thin Solid Films*, 2016, *615*, 128. [5] Kalita et. al. *Spolid State Ionics,* 2015, *229*, 14. [6] Nong et al. *Mat. Lett.* 2015, *154*, 167. [7] Tan et. al. *ECS Solid State Lett*, 2012, *1*, Q7. [8] Kazyak et al. *Chem Mat.* 2018, *29*, 3785. [9] Pfenninger Rupp et al. *Nature Energy*,2019, *1,* 475.)

Table S1. Parameters and chemicals for the first step of sequential decomposition synthesis of Li garnets.

Parameter	Value
Total volume of spray solution	5–15 mL
Flow rate of spray solution	5–20 mL/h
Concentration of spray solution	0.03 mol LLZO/L
Pressure at atomizer	0.3 bar
Distance between heated substrate and atomizer	24 cm
Hot-plate temperature	540 °C
Substrate temperature	280–330 °C
Carrier gas	compressed air
Spray solution (solutes)	$LiNO_3$ (10–250 mol.% excess) $La(NO_3)_3 \cdot 6H_2O$ $Zr(C_5H_7O_2)_4$ $Al(NO_3)_3 \cdot 9H_2O$
Spray solution (solvents)	33:33:33 vol%: methanol, 1-methoxy-2-propanol, and bis(2-ethylhexyl) phthalate

Supplementary References:

1. Kazyak, E.; Chen, K.-H.; Wood, K. N.; Davis, A. L.; Thompson, T.; Bielinski, A. R.; Sanchez, A. J.; Wang, X.; Wang, C.; Sakamoto, J.; Dasgupta, N. P., Atomic Layer Deposition of the Solid Electrolyte Garnet Li7La3Zr2O12. *Chemistry of Materials* **2017,** *29* (8), 3785-3792.
2. Garbayo, I.; Struzik, M.; Bowman, W. J.; Pfenninger, R.; Stilp, E.; Rupp, J. L. M., Glass-Type Polyamorphism in Li-Garnet Thin Film Solid State Battery Conductors. *Advanced Energy Materials* **2018,** *8* (12), 1702265 (14 pp.).
3. Sastre, J.; Priebe, A.; Döbeli, M.; Michler, J.; Tiwari, A. N.; Romanyuk, Y. E., Lithium Garnet Li7La3Zr2O12 Electrolyte for All-Solid-State Batteries: Closing the Gap between Bulk and Thin Film Li-Ion Conductivities. *Advanced Materials Interfaces* **2020,** *7* (17), 2000425.
4. Pfenninger, R.; Struzik, M.; Garbayo, I.; Stilp, E.; Rupp, J. L. M., A low ride on processing temperature for fast lithium conduction in garnet solid-state battery films. *Nature Energy* **2019,** *4* (6), 475-483.
5. Bitzer, M.; Van Gestel, T.; Uhlenbruck, S.; Hans Peter, B., Sol-gel synthesis of thin solid Li7La3Zr2O12electrolyte films for Li-ion batteries. *Thin Solid Films* **2016,** *615*, 128-134.
6. Chen, R.-J.; Zhang, Y.-B.; Liu, T.; Xu, B.-Q.; Shen, Y.; Lin, Y.-H.; Nan, C.-W., Improvement of the conductivity of sol-gel derived Li-La-Zr-O thin films by the addition of surfactant. *Ceramics International* **2017,** *43*, S603-S608.
7. Tadanaga, K.; Egawa, H.; Hayashi, A.; Tatsumisago, M.; Mosa, J.; Aparicio, M.; Duran, A., Preparation of lithium ion conductive Al-doped Li7La3Zr2O12 thin films by a sol-gel process. *Journal of Power Sources* **2015,** *273*, 844-7.
8. Moran Balaish, J. C. G.-R., Yuntong Zhu, Kun Joong Kim, Zachary D. Hood, Jennifer L.M. Rupp, *Nature Energy* **2020**.
9. van den Broek, J.; Afyon, S.; Rupp, J. L. M., Interface-Engineered All-Solid-State Li-Ion Batteries Based on Garnet-Type Fast Li+ Conductors. *Advanced Energy Materials* **2016,** *6* (19), 1600736 (11 pp.).
10. Matsuda, Y.; Matsui, M.; Imanishi, N., Phase transformation of garnet-type lithium-ion conductor Li7La3Zr2O12. *Netsu Sokutei* **2015,** *42* (2), 62-8.
11. Lobe, S.; Dellen, C.; Finsterbusch, M.; Gehrke, H. G.; Sebold, D.; Tsai, C. L.; Uhlenbruck, S.; Guillon, O., Radio frequency magnetron sputtering of Li7La3Zr2O12 thin films for solid-state batteries. *Journal of Power Sources* **2016,** *307*, 684-9.
12. Rawlence, M.; Filippin, A. N.; Wackerlin, A.; Lin, T. Y.; Cuervo-Reyes, E.; Remhof, A.; Battaglia, C.; Rupp, J. L. M.; Buecheler, S., Effect of Gallium Substitution on Lithium-Ion Conductivity and Phase Evolution in Sputtered Li7-3 xGaxLa3Zr2O12Thin Films. *ACS Applied Materials and Interfaces* **2018,** *10* (16), 13720-13728.
13. Kalita, D.; Lee, S.; Lee, K.; Ko, D.; Yoon, Y., Ionic conductivity properties of amorphous Li–La–Zr–O solid electrolyte for thin film batteries. *Solid State Ionics* **2012,** *229*, 14-19.
14. Marcinek, M.; Syzdek, J.; Marczewski, M.; Piszcz, M.; Niedzicki, L.; Kalita, M.; Plewa-Marczewska, A.; Bitner, A.; Wieczorek, P.; Trzeciak, T., Electrolytes for Li-ion transport–Review. *Solid State Ionics* **2015,** *276*, 107-126.
15. Nong, J.; Xu, H.; Yu, Z.; Zhu, G.; Yu, A., Properties and preparation of Li-La-Ti-Zr-O thin film electrolyte. *Materials Letters* **2015,** *154*, 167-169.
16. Tan, J.; Tiwari, A., Fabrication and characterization of Li7La3Zr2O12 thin films for lithium ion battery. *ECS Solid State Letters* **2012,** *1* (6), Q57-Q60.

17. Joong Sun, P.; Lei, C.; Zorba, V.; Mehta, A.; Cabana, J.; Guoying, C.; Doeff, M. M.; Richardson, T. J.; Jung Hoon, P.; Ji-Won, S.; Wan-Shick, H., Effects of crystallinity and impurities on the electrical conductivity of Li-La-Zr-O thin films. *Thin Solid Films* **2015,** *576*, 55-60.